A new neutron-gamma density measurement method using mass attenuation coefficient function*

Jun-Yan Chen[1] and Qiong Zhang[1, †]

[1]*University of Electronic Science and Technology of China, Chengdu 611731, China*

While traditional gamma-gamma density (GGD) logging technology is widely utilized, its potential environmental risks have prompted the development of more environmentally friendly neutron-gamma density (NGD) logging technology. However, NGD measurements are influenced by both neutron and gamma radiation. In the logging environment, variations in formation composition indicate different elemental compositions, which affect neutron-gamma reaction cross-sections and gamma generation. Compared to traditional gamma sources such as Cs-137, these changes can significantly impact the generation and transport of neutron-induced inelastic gamma rays, posing challenges for accurate measurements. To address this, a novel method is proposed, the method incorporates the mass attenuation coefficient function to account for the effects of various lithologies and pore contents on gamma-ray attenuation and therefore can achieve more accurate density measurements by clarifying the transport processes of inelastic gamma rays with varying energy and spatial distributions in varied logging environments. The method avoids the complex correction of the neutron transport and is verified through Monte Carlo simulations for its applicability across various lithologies and pore contents. showing that the absolute density errors are less than 0.02 g/cm^3 in clean formations and demonstrating good accuracy. The research not only clarifies the NGD mechanism but also provides theoretical guidance for the application of NGD logging methods. Further research will be conducted regarding extreme environmental conditions and tool calibration.

Keywords: Neutron-gamma density, Mass attenuation coefficient, Monte Carlo simulation

I. INTRODUCTION

In field of petroleum exploration, traditional gamma-gamma density (GGD) logging technology has played a crucial role for many years [1–5]. However, with growing awareness of environmental protection, the risks of pollution and operational safety associated with GGD technology have become increasingly apparent, posing challenges to its further development. In this context, neutron-gamma density (NGD) logging technology has emerged as new research focus due to its advantage of environmental protection and controllability [6–10]. GGD relies on the transport of monoenergetic gamma rays from the source to the detectors, while NGD is based on the transport of neutron-induced gamma rays, whose energy exhibits uncertainty. In NGD, the gamma rays detected by the detector are influenced by neutron transport from the neutron source to the point of the gamma ray producing neutron interaction in the formation and by the subsequent transport of the gamma rays from their source to the gamma-ray detector. To eliminate the influence of thermal neutron effects, density measurements are conducted using inelastic gamma rays produced by high-energy neutrons [11, 12]. Once neutrons are emitted, they undergo inelastic scattering reactions with isotopes of crucial elements in the medium in a few microseconds, producing inelastic gamma rays. These gamma rays are less influenced by neutron transport, enabling them to more accurately reflect formation characteristics, making them more suitable for density measurements. However, evaluating inelastic gamma rays can be tricky because it depends on both neutron and gamma physics and undergoes multiple physics processes simultaneously. Hence in this case, the entanglement between neutron and gamma transport increases the complexity of the measurement and its sensitivity to its environment. The generation and attenuation of inelastic gamma rays are directly influenced by environment factors such as lithology, porosity, and fluid properties. It is critical to understand both neutron and gamma physics pertaining to changing environments in order to develop an accurate method for NGD technology [13–15].

The development of neutron-gamma density (NGD) technology has been actively ongoing for the past few decades. For instance, Odom et al. used inelastic gamma rays for density measurements, which advanced density logging technology based on the neutron-gamma coupled field theory [16, 17]. However, this method is affected by neutron transport, and neutron transport correction needs to be considered in subsequent studies. Jacobson et al. developed a correction technique that employs capture gamma count ratio to obtain a compensated inelastic gamma ratio, achieving the density measurements [18]. Zhang et al. developed a density method by using the inelastic gamma-count ratio and the fast-neutron count to avoid neutron correction [19]. Luycx et al. approximated the initial inelastic gamma flux by fast neutron counts for density measurements [20].Wang et al. created a correction model utilizing epithermal neutrons, and divided the inelastic gamma-ray energy spectrum into high- and low-energy windows to reduce the influence of Pair production [21]. Additionally, Zhang et al. introduced an adaptive method for obtaining inelastic gamma spectra while environment changes and integrated capture correction for density measurement [22]. While these studies have made progress, most researchers focused more on analyzing the neutron transport process and less on the dynamic changes in gamma attenuation process. Inelastic gamma rays generated by neutron-induced reactions exist in formations in a non-

* Supported by the Natural Science Foundation of China U23B20151 and 52171253

† Corresponding author, Qiong Zhang, University of Electronic Science and Technology of China, Chengdu 611731, China (e-mail: zhanqio@uestc.edu.cn)

monoenergetic distribution, whereas chemical sources like Cs-137 generate monoenergetic gamma in a homogeneous manner. Furthermore, typical neutron-induced gamma rays can reach energies up to 8 MeV [23]. Pair production needs to be considered as it plays a vital role in the neutron-induced gamma transport process. These factors contribute to the complexity of gamma attenuation. Previous neutron-gamma density (NGD) and gamma-gamma density (GGD) provide possibilities for density measurements. However, most of previous NGD methods consider mass attenuation coefficient as a constant, this limits the accuracy because it is closely related to the formation composition. In our work, we introduce mass attenuation coefficient as a function related to formation lithologies and pore contents, in order to accurately depict the intricate interaction mechanisms between radiation and formation, which is essential in obtaining accurate formation density. This can also provide a new approach to complement previous methods.

The manuscript is organized as follows: Section 2 introduces the method and presents the development process. Also, a pulsed neutron density tool is described, which later is employed for concept verification. Section 3 presents the results from different simulated scenarios, demonstrating the method's effectiveness. Finally, Conclusions are drawn in Section 4.

II. METHOD

The development of the method is shown in Fig.1: Box1 reviews the coupled field theory of neutron-gamma density (NGD) measurement, which is the foundation for the proposed method as it depicts inelastic gamma rays' distribution. Box2 is key to the method: a function for mass attenuation coefficient is developed, which is then used to derive density. Certain key parameters, such as the hydrogen index cannot be directly expressed in this mathematical form, instead, they are obtained through tool measurement. Box3 presents analysis of physical parameters using a real NGD tool under development stage. Extensive Monte Carlo simulations are conducted to establish a quantitative relationship between detector responses and formation physical parameters, which is consequently utilized to obtain these key parameters. Finally, density is calculated. Overview of the method is illustrated in Fig.1.

A. Coupled field theory of NGD Measurement

NGD logging technology relies on inelastic gamma rays to measure formation density [24–29]. The distribution of inelastic gamma rays involves two interconnected links of neutron and gamma transport [30–32]. Detailed process is discussed as below:

The pulsed neutron source emits 14MeV fast neutrons. In a spherical model, according to neutron diffusion theory, the distribution of fast neutrons can be described as follows:

$$\Phi_n = \frac{Q}{4\pi D_n r}\exp(-\frac{r}{L_n}) \tag{1}$$

where Q is the number of neutrons emitted by the neutron source per second, D_n is the neutron diffusion coefficient, L_n is the fast neutron deceleration length, and r is the distance between the pulsed neutron source and the neutron detector. The inelastic gamma rays recorded by a detector with a radius R, can be described by the following equation [21]:

$$\Phi_{in}(R) = \frac{i\Sigma_{in}Q\int_0^\infty \exp(-\frac{r}{L_n}\exp(-\rho\mu_m\left|r-R\right|)dr}{4\pi D_n R}) \tag{2}$$

where i is the average number of inelastic gamma rays after neutron enters the formation, Σ_{in} is the inelastic scattering cross section, ρ is the formation density, and μ_m is the total mass attenuation coefficient. The inelastic gamma rays within the distance from the source R are recorded [33], and Eq.(2) can be written as:

$$\Phi_{in}(R) = \frac{i\Sigma_{in}Q}{4\pi D_n R}\frac{\exp(-\frac{R}{L_n}) - \exp(-\rho\mu_m R)}{\rho\mu_m - \frac{1}{L_n}} \tag{3}$$

According to the Lagrange interpolation method, Eq.(3) can be simplified as follows:

$$\Phi_{in}(R) = \frac{i\Sigma_{in}Q}{4\pi D_n}\exp(-R\xi) \tag{4}$$

where ξ belongs to $(\rho\mu_m, \frac{1}{L_n})$, which can be written as: $\xi = \frac{1}{L_n} - \alpha(\frac{1}{L_n} - \rho\mu_m), \alpha \in (0,1)$.

Assuming that the source distances of the near and far gamma detectors are $L1$ and $L2$ ($L1 < L2$), the following equations can be obtained:

$$\begin{cases}\Phi_{in}(L_1) = \frac{i\Sigma_{in}Q}{4\pi D_n}\exp(-L_1\xi_1)\\ \Phi_{in}(L_2) = \frac{i\Sigma_{in}Q}{4\pi D_n}\exp(-L_2\xi_2)\end{cases} \tag{5}$$

where:

$$\begin{cases}\xi_1 = \frac{1}{L_n} - \alpha_1(\frac{1}{L_n} - \rho\mu_m), \alpha_1 \in (0,1)\\ \xi_2 = \frac{1}{L_n} - \alpha_2(\frac{1}{L_n} - \rho\mu_m), \alpha_2 \in (0,1)\end{cases} \tag{6}$$

The logarithm of ratio of near and far inelastic gamma counts is as follows:

$$\begin{aligned}\ln(RIN) &= \ln(\frac{\Phi_{in}(L_1)}{\Phi_{in}(L_2)})\\ &= \frac{L_1\alpha_1 - L_2\alpha_2 + L_2 - L_1}{L_n} + (L_2\alpha_2 - L_1\alpha_1)\rho\mu_m\end{aligned} \tag{7}$$

Suppose $a = L_1\alpha_1 - L_2\alpha_2 + L_2 - L_1$, $b = L_2\alpha_2 - L_1\alpha_1$,Eq.(7) can be reorganized:

$$ln(RIN) = \frac{a}{L_n} + b\rho\mu_m \tag{8}$$

Eq. (8) shows that the response of gamma-ray detector is related to the L_n, ρ, μ_m, and the value of a, b. The fast neu-

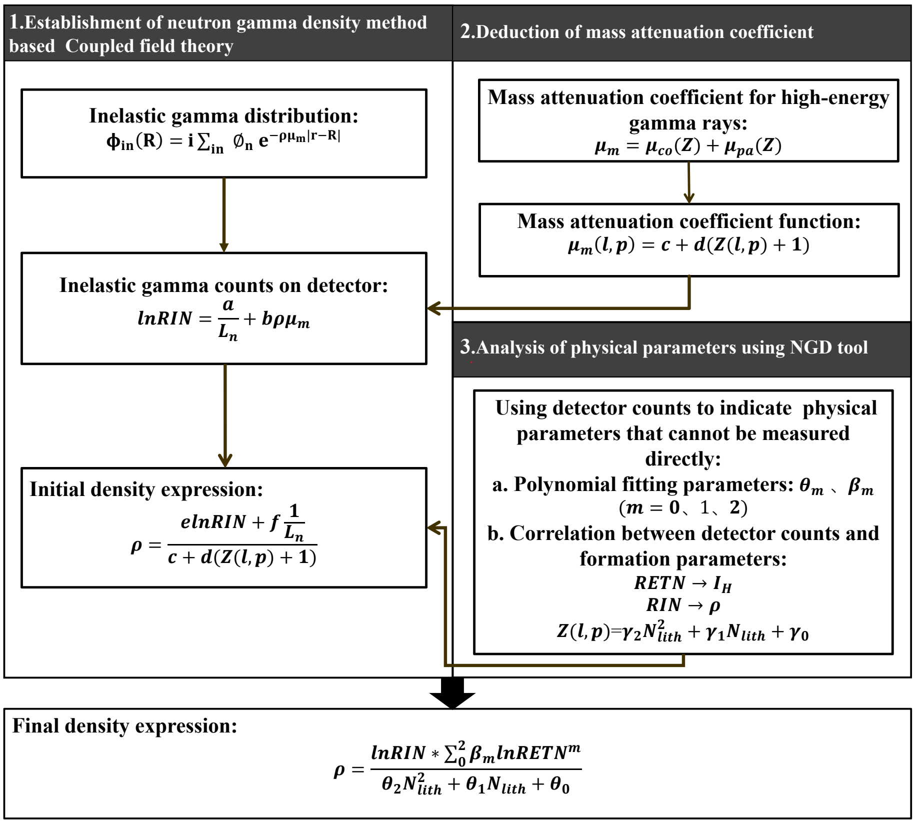

Fig. 1. (Color online) Overview of the proposed method

tron deceleration length, L_n in typical formations can be characterized by the formation density ρ, the hydrogen index I_H, and the initial energy of fast neutron E_0 [34]:

$$L_n = k\sqrt{\frac{1}{I_H + c}}\sqrt{\frac{1}{\rho}}\sqrt{ln(E_0)} \tag{9}$$

The key parameter in Eq.(8) is the mass attenuation coefficientμ_m, which directly reflects the attenuation of gamma rays in formations. The section below will focus on analyzing this parameter.

B. NGD method development

The attenuation of gamma rays in formations is closely linked to formation density and the mass attenuation coefficient. This attenuation process is primarily influenced by various physics processes, including the Photoelectric effect, Compton effect, and Pair production. Especially for high-energy gamma rays, Compton effect and Pair production are the main factors affecting their attenuation. Thus, the total attenuation coefficient μ_m can be expressed as follows:

$$\mu_m = \mu_{co} + \mu_{pa} \tag{10}$$

where μ_{co} is the mass attenuation coefficient for Compton effect, μ_{pa} is the mass attenuation coefficient for pair production.

According to the principles of Compton effect and Pair production [35, 36], the mass attenuation coefficient of Compton effect and Pair production can be expressed as:

$$\begin{aligned}\mu_{co} =& 2\pi(r_0)^2\{\frac{1+\eta}{\eta^2}\left[\frac{2(1+\eta)}{1+2\eta} - \frac{1}{\eta}\ln(1+2\eta)\right] \\ &+ \frac{1}{2\eta}\ln(1+2\eta) - \frac{1+3\eta}{(1+2\eta)^2}\}N_A\frac{Z}{A}\end{aligned} \tag{11}$$

$$\mu_{pa} = \frac{(r_0)^2 N_A}{137}(\frac{28}{9}\ln(2\eta) - \frac{218}{27})(Z+1)\frac{Z}{A} \tag{12}$$

where N_A is Avogadro constant, r_0 is the classical electron radius (r_0=2.818*10-13cm), $\eta = \frac{E_\gamma}{m_e c^2}$, E_γ is the gamma-ray energy, m_e is the electron rest mass(m_e=9.110*10-31kg), c is the speed of light in a vacuum (c=2.998*108m/s), Z is the atomic number, A is the atomic weight. The total mass attenuation coefficient can be rewritten as:

$$\begin{aligned}\mu_m =& \pi(r_0)^2\{\frac{1+\eta}{\eta^2}\left[\frac{2(1+\eta)}{1+2\eta} - \frac{1}{\eta}\ln(1+2\eta)\right] \\ &+ \frac{1}{2\eta}\ln(1+2\eta) - \frac{1+3\eta}{(1+2\eta)^2}\}N_A \\ &+ \frac{(r_0)^2 N_A}{274}(\frac{28}{9}\ln(2\eta) - \frac{218}{27})(Z+1)\end{aligned} \tag{13}$$

Eq.(13) shows the impact of gamma-ray energyE_γ,and formation atomic number Z on the mass attenuation coefficient μ_m , highlighting the response sensitivity among these variables. This work emphasizes the variability of the mass attenuation coefficient, which is different to previous studies where the mass attenuation coefficient was typically assumed to be constant. While changes in the mass attenuation coefficient within the average energy range of inelastic gamma rays in formations are small enough to have the effect of gamma energy ignored [37]. Instead, its close correlation with the formation's composition is emphasized, particularly the effects of lithology and pore content on the macroscopic atomic number(Z). To further prove this point, Fig.2 is shown which represents the difference in formation's macroscopic atomic numbers when the lithology and porosity content change. These changes in lithology and pore content indicate variations in the constituent elements of the formation, which directly affect the formation macroscopic atomic number(Z), resulting in alterations to the total mass attenuation coefficient. This affects gamma rays' attenuation, thereby complicating gamma-ray transport. So, the mass attenuation coefficient is treated as a function related to the formation lithology(l) and pore content(p). Accurate measurement of density can be achieved by describing the influence of different formation components on the gamma transport process.

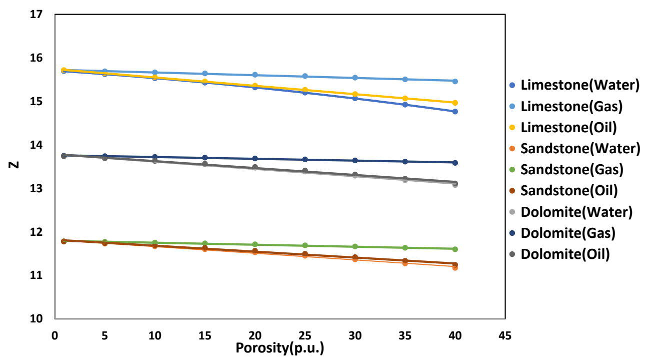

Fig. 2. (Color online) Z-results across different formations with various pore contents

According to the above analysis, treating mass attenuation coefficient as a function pertaining to environmental parameters will better depict gamma-formation reaction sensitivity and thus enable more accurate NGD calculations:

$$\mu_m(l,p) = c + d(Z(l,p)+1) \tag{14}$$

$$\begin{aligned} c =& \pi(r_0)^2 N_A\{\frac{1+\eta}{\eta^2}\left[\frac{2(1+\eta)}{1+2\eta} - \frac{1}{\eta}\ln(1+2\eta)\right] \\ &+ \frac{1}{2\eta}\ln(1+2\eta) - \frac{1+3\eta}{(1+2\eta)^2}\} \end{aligned} \tag{15}$$

$$d = \frac{(r_0)^2 N_A}{274}(\frac{28}{9}\ln(2\eta) - \frac{218}{27}) \tag{16}$$

where c and d are constants.

After substituting the mass attenuation coefficient μ_m from Eq.(14) into Eq.(8), the equation can be reformulated as follows:

$$\rho = \frac{e\ln(RIN) + f\frac{1}{L_n}}{c + d(Z(l,p)+1)} \tag{17}$$

This expression is composed of 2 key parameters: the fast neutron deceleration length L_n and the formation's macroscopic atomic number Z, and L_n is related to the formation density and the hydrogen index. These physical parameters cannot be directly measured, instead, they can be derived through the analysis of detector responses. Consequently, in the next section, we present a real pulse neutron logging tool and construct a high-fidelity Monte Carlo model for the analysis of these physical parameters.

C. Analysis of physical parameters using NGD tool

Geant4 (Geometry and Tracking 4), an open-source Monte Carlo platform, is used for simulations. The tool model, shown in Fig.3, has a total length of 2328 mm and a diameter of 188 mm, featuring four neutron detectors and two gamma detectors. To minimize the impact of water in the mud pipe on neutron detection, a boron-containing shield is positioned at the base of the neutron detectors. Additionally, the near gamma detector is used not only for density measurement but also for formation sigma and elemental measurements. To reduce interference from capture gamma rays generated by the tool's interaction with thermal neutrons, a two-layer shielding structure is implemented. A cubic space measuring 6 * 6 * 6m is designated to simulate formation environment, with a borehole diameter of 215.9 mm, positioning the tool at the center of the borehole. This tool is currently undergoing construction and will be deployed in the field upon completion. Therefore, it is selected to verify the feasibility of the proposed method. Extensive simulations are conducted using a NGD tool model, incorporating various formation lithologies (limestone, sandstone, dolomite) and porosity ranges (0-40 p.u.). These simulations aim to establish the relationship between detector responses and relevant physical parameters in the Eq. (17) and therefore will be used for concept validation. The specific relationships are as follows:

(a) Hydrogen index(I_H)

The correlation between hydrogen index and detector responses is analyzed using simulation data. Fig.4(a) presents the correlation coefficients between various detector responses and hydrogen index. These coefficients measure the strength of the linear relationship between the variables, with values closer to 1 indicating a strong correlation. This analysis helps identify the optimal response for representing the hydrogen index. In Fig.4(a), the features represent various detector counts: $FN1$ and $FN2$ correspond to near and far fast neutron counts, $ETN1$ and $ETN2$ to near and far epithermal neutron counts, and $CAP1$ and $CAP2$ to near and far capture gamma counts. Additionally, RFN, $RETN$, and $RCAP$ represent the respective ratios of fast neutrons, epithermal neutrons, and capture gamma counts. As shown in

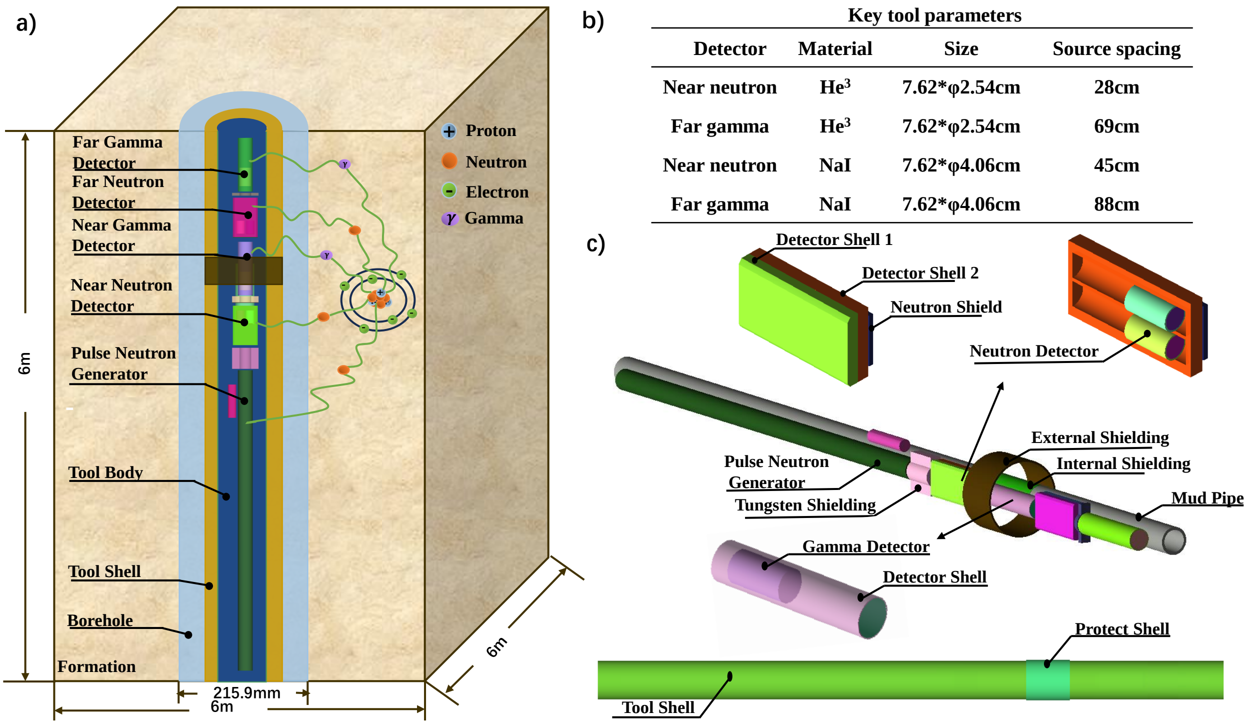

Key tool parameters

Detector	Material	Size	Source spacing
Near neutron	He^3	7.62*φ2.54cm	28cm
Far gamma	He^3	7.62*φ2.54cm	69cm
Near neutron	NaI	7.62*φ4.06cm	45cm
Far gamma	NaI	7.62*φ4.06cm	88cm

Fig. 3. (Color online) Tool model: (a)tool overview; (b) key tool parameters; (c) shielding structure

the figure, the ratio of near to far epithermal neutron counts ($RETN = ETN1/ETN2$) exhibit the strongest correlation with the hydrogen index, making $RETN$ the most effective indicator of hydrogen content among all detector responses.

(b) Formation density(ρ)

To accurately represent formation density, correlation analysis is applied to evaluate the relationships between various detector responses and density. In Fig. 4(b), $IN1$ and $IN2$ represent near and far inelastic gamma counts, while $CAP1$ and $CAP2$ represent near and far capture gamma counts. RIN is the ratio of near to far inelastic gamma counts, expressed as $RIN = IN1/IN2$.And $RCAP$ is the ratio of near to the far capture gamma counts. As shown in Fig.4(b), RIN exhibits the strongest correlation with density, making it the optimal parameter for describing density in Eq. (9). This is also consistent with NGD physics principle [38, 39].

(c) Formation macroscopic atomic number(Z)

The macroscopic atomic number Z, an inherent characteristic of the formation, is closely influenced by lithology and pore contents. By analyzing the detector counts within a specific energy window (0.07 to 0.35 MeV), denoted as N_{lith}, a relationship can be established to represent macroscopic atomic number. As shown in Fig. 4(c), this method allows for the derivation of Z from the detector responses, using counts within the designated energy range to effectively characterize the formation's macroscopic atomic number.

To summarize, density, hydrogen index and formation macroscopic atomic number Z can be represented using RIN, $RETN$ and N_{lith}, all of which can be obtained from detector counts. Since the root term in the represented equation complicates the acquisition of calibration coefficients, a polynomial fit approach was used to simplify the equation,as shown in Fig.4(d). After substituting the root term with a second-degree expression, previous Eq.(9) can be rewritten as:

$$L_n = \frac{\tau_0}{\tau_1 \ln(RIN) * \sum_0^2 t_m(\ln(RETN))^m} \tag{18}$$

By substituting the L_n expression into Eq. (17), density equation can be obtained:

$$\rho = \frac{\ln(RIN) * \sum_0^2 \beta_m(\ln(RETN))^m}{\theta_2(N_{lith})^2 + \theta_1 N_{lith} + \theta_0} \tag{19}$$

where β_0, β_1, β_2, θ_0, θ_1, θ_2 is the fitting parameter. From Eq. (19), the formation density is determined by three parameters: the ratio of inelastic gamma counts RIN, the ratio of epithermal neutron counts $RETN$, and the count N_{lith}. The coefficients in the above equation using the Levenberg-Marquardt method are obtained.

III. RESULTS AND DISCUSSIONS

To prove the effectiveness of developing mass attenuation coefficient function, we compare two approaches for treating the mass attenuation coefficient: as a constant versus as a function of formation composition. The results demonstrate that treating it as a function can significantly enhance calculation accuracy, demonstrating the effectiveness of the method. Next, we assess the method's performance across various environments, focusing on two critical factors: formation lithol-

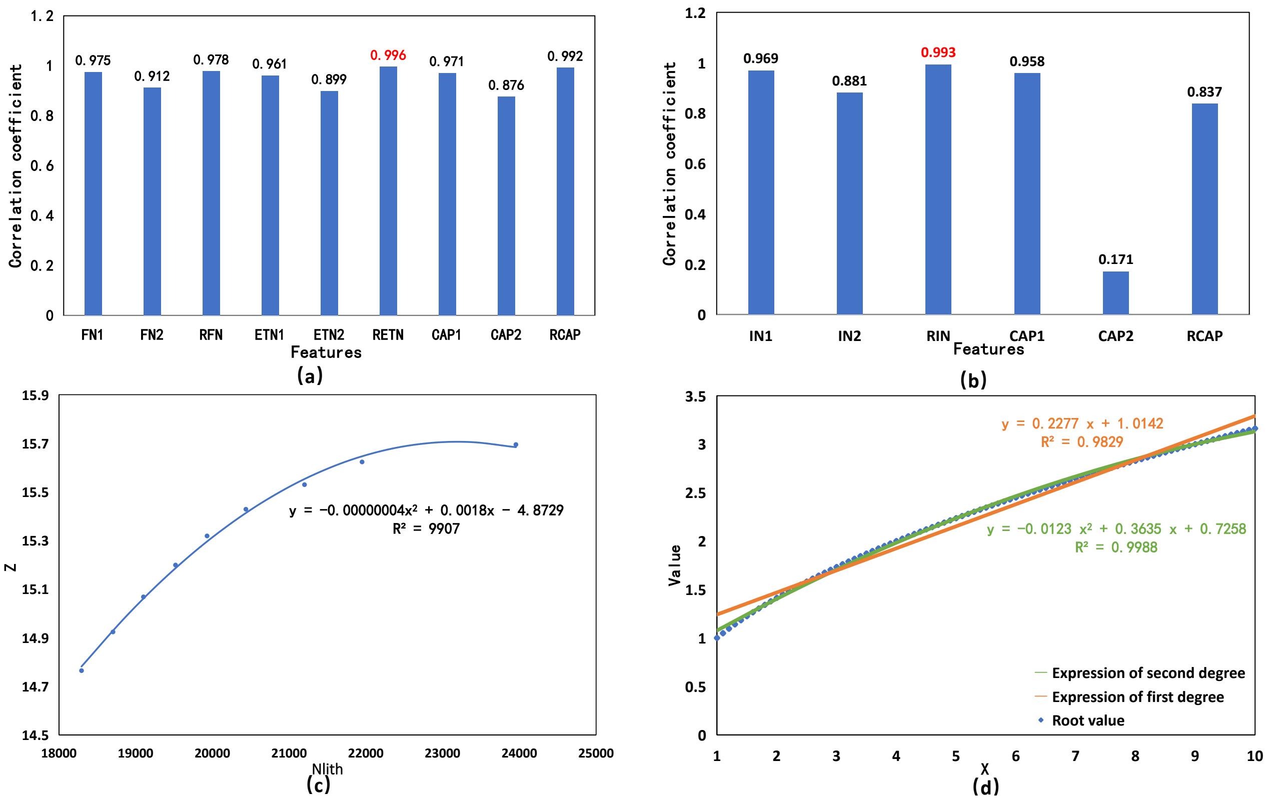

Fig. 4. (Color online) Analysis of physical parameters: (a) Hydrogen Index; (b) Density; (c) Limestone's Macroscopic Atomic Number; (d) Polynomial fit

ogy and pore content. Finally, we present three test cases to validate the method's applicability in complex formations. The absolute errors are used to evaluate the calculated density results, as expressed in Eq. (19). When the absolute errors are less than the threshold of 0.025 g/cm^3, the calculated results are considered accurate [40].

$$Error = |DT - DC| \tag{20}$$

where Error is the absolute error between calculated density(DC) and true density of the simulated formation(DT).

A. Comparison of two approaches regarding mass attenuation coefficient

Section 2.2 emphasizes that the proposed method treats the mass attenuation coefficient as a function pertaining to formation lithology and pore content. To evaluate the effectiveness of this method, a comparison is conducted in this section, primarily focusing on two approaches of the mass attenuation coefficient: treating it as a constant (denoted as h) versus treating it as a function. Based on Eq. (8) and the analysis of the relevant physical parameters in Section 2.3, if the mass attenuation coefficient is treated as h, the equation can be obtained:

$$\rho = \frac{\ln(RIN) * \sum_0^2 \beta_m (\ln(RETN))^m}{h} \tag{21}$$

where β_0, β_1, β_2 and h are the fitting parameters. From Eq. (19), the density is determined by two parameters: the ratio of inelastic gamma counts RIN and the ratio of epithermal neutron counts $RETN$.

Limestone with densities ranging from 2.018 g/cm^3 to 2.862 g/cm^3 are designed to compare two approaches. Fig. 5(a) presents the absolute density errors of both approaches. The results clearly illustrate significant differences: the constant method has a relatively high average absolute error of 0.048 g/cm^3, whereas the error calculated by the proposed method is reduced by about four times compared to the constant method, with an average absolute error of 0.012 g/cm^3. This demonstrates the effectiveness and accuracy of the new method in measuring formation density.

B. Pore content impact analysis

In neutron gamma density(NGD) measurements, neutron transport is sensitive to the presence of pore content. To evaluate the impact of different pore contents on the accuracy of this method, limestone with porosities ranging from 0.9 to 40 p.u. are selected, with pores filled with water, gas, or oil. The density results under different pore contents are shown in Ta-

ble 1 and Fig.5 (b).

TABLE 1. Density results across different pore fluids

Porosity (p.u.)	Water(1.0 g/cm^3) Error (g/cm^3)	Gas(0.2 g/cm^3) Error (g/cm^3)	Oil(0.835 g/cm^3) Error (g/cm^3)
0.9	0.010	0.003	0.005
10	0.005	0.007	0.019
20	0.002	0.003	0.007
25	0.003	0.012	0.020
30	0.006	0.011	0.010
35	0.008	0.011	0.012
40	0.008	0.005	0.012

Table 1 and Fig.5(b) present the density calculation results for varying pore contents. For analysis, seven porosity types are selected, each tested under conditions where the pores are filled with water, oil, and gas. In limestone with pores filled with water, the Hydrogen Index I_H is equivalent to the formation's porosity. The results indicate that the I_H has a minimal impact on density measurements. Regardless of I_H variations, the errors between calculated densities and true densities are less than the threshold of 0.025g/cm^3, demonstrating that densities calculated by the new method consistently align well with true densities. Additionally, the method can also achieve accurate measurements in high I_H formations. When comparing density calculations for different pore contents, it is observed that when the pores are filled with water or gas, the absolute density errors are relatively small, remaining below 0.015g/cm^3. However, the errors are relatively large when the pores are filled with oil. Notably, whether the pores are filled with water, oil, or gas, the absolute errors are less than 0.02 g/cm^3. This demonstrates that the method can accurately calculate formation density across various porosities and pore contents.

C. Lithology impact analysis

Since different lithologies affect neutron transport and gamma attenuation, 42 models, including limestone, sandstone, dolomite, and one-to-one mixture of any two lithologies, are designed to verify the accuracy of the proposed method. All model pores are filled with water, with porosities ranging from 0.9 to 40 p.u. The densities calculated using the proposed method are compared with true densities used in simulated model construction, which varied between 1.93 g/cm^3 and 2.843 g/cm^3. The density results are shown in Fig.5(c) and Table 2.

To verify the impact of lithology on density measurement, the study focuses on two types of formations: single lithology (clean formations) and mixed lithology composed of sandstone, limestone, and dolomite. As shown in Fig.5(c) and Table 2, there are slight differences in density results across various lithologies, and the average absolute error in mixed lithology is slightly larger than that in single lithology, likely due to the complexity of the formation's composition. Whether it is a single lithology or a mixed lithology, the calculated densities closely align with the true densities, and the absolute density errors less than 0.02 g/cm^3. Overall, the average absolute error in the test database is 0.009g/cm^3, confirming the accuracy of the proposed method under different lithologies.

D. Multi-parameter impact analysis

The above results quantitatively analyze the impact of lithology and pore content on the accuracy of the density measurement. To further evaluate the proposed method, three cases (Case 1, Case 2, and Case 3) are designed, representing three lithologies (limestone, sandstone, dolomite) and three pore contents (water, oil, gas), while considering mud components (such as chlorite). Specifically, Case 1 simulates a water-filled limestone with 20% chlorite, Case 2 simulates an oil-filled sandstone with 10% chlorite, and Case 3 simulates dolomite containing gas, which has a relatively high chlorite content of 40%. In all cases, the borehole size is 8.5 inches, with a porosity range set from 0 to 25 p.u., and formation densities between 2.211 g/cm^{3}and 2.712 g/cm^3. The results are illustrated in Fig.6.

From Fig.6, the inelastic gamma ratio and epithermal neutron ratio vary across formations with different lithologies and pore contents, highlighting the impact of formation composition on neutron transport and gamma attenuation. In particular, Case 1 and Case 2 exhibit smaller measurement errors, demonstrating higher accuracy. In contrast, Case 3 exhibits relatively higher measurement errors, possibly due to its more complex formation composition characterized by elevated mud content and gas-filled pores. Nevertheless, the absolute density errors in all three cases remain below 0.02 g/cm ^{3}, demonstrating the accuracy and reliability of the proposed method for measuring formation density.

IV. CONCLUSIONS

(1) A new mass attenuation coefficient function of formation lithology and pore content is introduced. Based on neutron induced gamma attenuation process study, mass attenuation coefficient is shown varying pertaining to formation parameters, therefore, this work proposes to consider it as a function to better evaluate the effects of environmental variables regarding gamma attenuation.

(2) A new density measurement method is developed by employing the concept of mass attenuation coefficient function that evaluates the effects of formation composition on gamma attenuation. The method relies on inelastic gamma rays for density measurement while incorporating epithermal neutrons to correct neutron transport, for example, fast neutron influences on spatial distribution and intensity of inelastic gamma rays. By integrating information from both neutrons and gamma rays, this method can evaluate interaction mechanisms between radiation and formation more accurately and therefore helps obtain more precise density measurement.

TABLE 2. Density results across different lithologies

Porosity (p.u.)	Limestone(g/cm^3)		Sandstone(g/cm^3)		Dolomite(g/cm^3)	
	True Density	Error	True Density	Error	True Density	Error
0.9	2.682	0.010	2.682	0.011	2.843	0
10	2.527	0.005	2.485	0.011	2.767	0.001
20	2.358	0.002	2.320	0.011	2.674	0.001
25	2.273	0.003	2.238	0.009	2.488	0.002
30	2.188	0.006	2.155	0.007	2.395	0.001
35	2.103	0.008	2.073	0.005	2.209	0.010
40	2.018	0.008	1.990	0.009	2.116	0.003
Porosity (p.u.)	Limestone+Sandstone(g/cm^3)		Limestone+Dolomite(g/cm^3)		Sandstone+Dolomite(g/cm^3)	
	True Density	Error	True Density	Error	True Density	Error
0.9	2.658	0.011	2.763	0.019	2.739	0.007
10	2.506	0.011	2.601	0.016	2.580	0.004
20	2.339	0.019	2.423	0.004	2.404	0.007
25	2.255	0.005	2.334	0.005	2.316	0.014
30	2.172	0.003	2.245	0.011	2.229	0.020
35	2.088	0.005	2.156	0.015	2.141	0.006
40	2.004	0.014	2.067	0.006	2.053	0.007

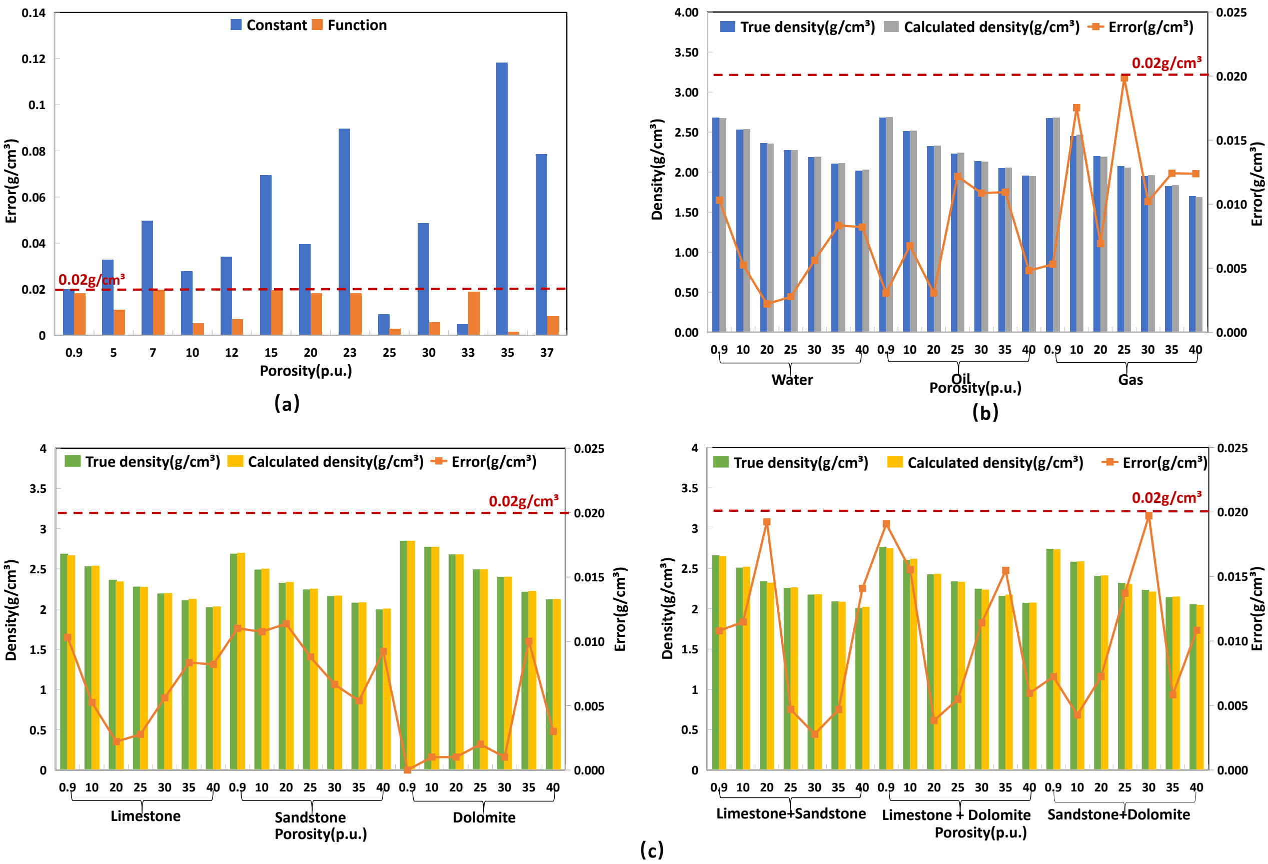

Fig. 5. (Color online) Density results: (a) Two approaches comparison; (b) Pore content results; (c) Lithology results

(3) An elaborate NGD tool model is built and employed to verify the performance of the new method. The proposed method is evaluated using a total of 63 sets of simulated models of varying lithologies and pore contents. The results show that the absolute errors of density calculated by the method are below 0.02 g/cm ^{3}for all cases. Specifically, the method obtains the same level of accuracy in mixed cases, proving its effectiveness. This can offer theoretical support for the design of new NGD tools. The method faces challenges in terms of extreme environmental conditions and tool calibration. For example, under logging-while-drilling

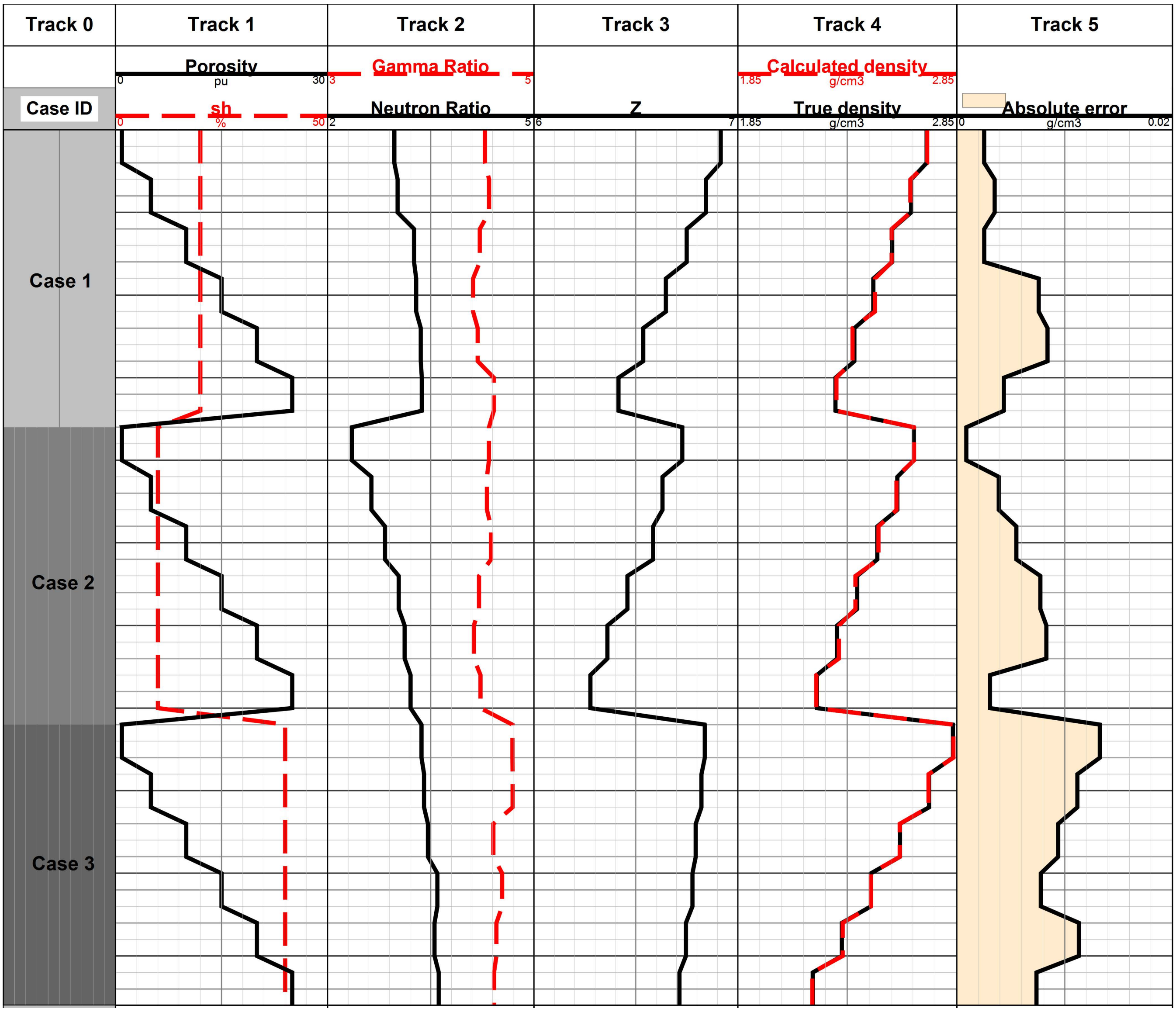

Fig. 6. (Color online)Results and comparisons. Track 0: Three cases, of which Case 1is limestone filled with water, Case 2 is sandstone filled with oil, and Case3 is dolomite filled with gas. Track 1: Case parameters, including porosity and mud content in the formation. Track 2: Detector counts, including the inelastic gamma count ratio $LNRIN$, and the epithermal neutron count ratio $LNRETN$. Track 3: Formation's macroscopic atomic number. Track 4: Comparison of the true density with the calculated density. Track 5: Absolute error.

downhole conditions such as high temperature (150°C) and high pressure (2000 psi), the performance of the tool 's detectors and electronics may be affected, while changes in the physical properties of borehole fluids can also occur, thus impacting measurement accuracy. Additionally, the method relies on significant amounts of calibration coefficients, this requires high-level calibration standards in tool-specific environments. To improve the applicability of the method, further in-depth research will be conducted regarding these two aspects.

FUNDING

This work was supported by the Science Foundation of China U23B20151 and 52171253.

NOMENCLATURE

μ_m	Total mass attenuation coefficient
μ_{co}	Mass attenuation coefficient for Compton effect
μ_{pa}	Mass attenuation coefficient for Pair production
ϕ_n	Fast neutron distribution

Φ_{in}	The inelastic gamma-rays distribution
ρ	Formation density
Σ_{in}	Inelastic scattering cross-section
A	The atomic weight
c	The speed of light in a vacuum
$CAP1$	Near captured gamma count
$CAP2$	Far captured gamma count
D_n	Neutron diffusion coefficient
DC	Calculated density
DT	True density of the simulated formation
E_0	Initial energy of fast neutron
E_γ	Gamma-ray energy
$ETN1$	Near epithermal neutron count
$ETN2$	Far epithermal neutron count
$FN1$	Near fast neutron count
$FN2$	Far fast neutron count
GGD	Gamma-gamma density
i	The average number of inelastic gamma rays after neutron enters the formation
I_H	Hydrogen index
$IN1$	Near inelastic gamma count
$IN2$	Far inelastic gamma count
l	Formation lithology
L_n	Fast neutron deceleration length
L_1	The distance of near gamma detector
L_2	The distance of far gamma detector
m_e	The electron rest mass
N_A	Avogadro's constant
NGD	Neutron-gamma density
p	Pore content
Q	The number of neutrons emitted per second
r	The distanc between source and detector
r_0	The classical electron radius
$RCAP$	Ratio of near to far capture gamma counts
$RETN$	Ratio of near to far epithermal neutron counts
RFN	Ratio of near to far fast neutron counts
RIN	Ratio of the near to far inelastic gamma counts
$Sigma$	Formation macroscopic capture cross section
Z	Atomic number

REFERENCES

[1] R. Spross, T. Burnett, J. Freeman et al., Formation Density Measurement While Drilling. In: SPWLA 34th Annual Logging Symposium. (Alberta, 1993). doi:10.30632/SPWLA-1993-PP

[2] Q. Zhang, Y. Wang, Formation density and photoelectric index calculation using an ultra-slim density tool. Geo. Sci. Eng. **237**, 212817 (2024). doi:10.1016/J.GEOEN.2024.212817

[3] Y.L. Li, Q. Zhang, A novel constraint-based method for density measurement in cased hole. Geo. Sci. Eng. **228**, 211954 (2023). doi:10.1016/J.GEOEN.2023.211954

[4] X.Y. Wang, Q. Zhang, High-efficiency Monte Carlo simulation based on CADIS method for Gamma Density Measurement. Ann. Nucl. Energy. **185**, 109710 (2023). doi:10.1016/j.anucene.2023.109710

[5] Q. Zhang, Y.L. Li, Y. Jin et al., A new gamma density measurement method for cased-hole formation evaluation. Appl. Radiat. Isot. **184**, 110178 (2022). doi:10.1016/j.apradiso.2022.110178

[6] H.W. Yu, Y.X. Zhang, X.H. Chen et al., Numerical simulation and method study of X-ray litho-density logging. Nucl. Sci. Tech. **31** (12), 124 (2020). doi:10.1007/s41365-020-00826-2

[7] Y. Ge, J. Liang, Q. Zhang et al., A comparison study of GEANT4 and MCNP6 on neutron-induced gamma simulation. Appl. Radiat. Isot. **190**, 110514 (2022). doi:10.1016/j.apradiso.2022.110514

[8] T. Gjerdingen, J. Hilton, N. Bounoua et al., Sourceless Neutron-Density Porosity Determination: Fit-for-Purpose Formation Evaluation with Significant HS&E Benefits. In: SPE Annual Technical Conference and Exhibition. (Texas, 2012). doi:10.2118/159522-MS

[9] G. Schmid, R. Pemper, D. Dolliver et al., A diffusion-corrected sigma algorithm for a four-detector pulsed-neutron logging tool. In: SPE Annual Technical Conference and Exhibition. (Texas, 2018). doi:10.2118/191738-MS

[10] J. Liu, S. Liu, S. Zhang et al., A method for evaluating gas saturation with pulsed neutron logging in cased holes. J. Nat. Gas. Sci. Eng. **59**, 354-362 (2018). doi:10.1016/j.jngse.2018.09.018

[11] F. Zhang, Q.Y. Zhang, J.T. Liu et al., A method to describe inelastic gamma field distribution in neutron gamma density logging. Appl. Radiat. Isot. **129**, 189-195 (2017).

doi:10.1016/j.apradiso.2017.08.024
[12] H. Wang, A.Z. Yue, X.L. Zhang et al., Bulk Density Response and Experimental Study of Pulsed Neutron-gamma density Logging. Front. Earth. Sci. **10** (2022). doi:10.3389/FEART.2022.803775
[13] Q.Y. Zhang, R. Deng, S.Q. Zhang et al., An alternative method for sourceless density measurement with boron sleeve gamma detectors. Appl. Radiat. Isot. **174**, 109785 (2021). doi:10.1016/j.apradiso.2021.109785
[14] M. Luycx, T.V. Carlos, Rapid forward modeling of logging-while-drilling neutron-gamma density measurements. Geophysics. **83** (6), D231-D246 (2018). doi:10.1190/geo2018-0142.1
[15] L. Zhang, H.W. Yu, W.B. Jia et al., Study on the influence of formation factors on spatial distribution of D-D induced γ-ray source. Nucl. Tech. **42** (1), 010501 (2019). doi:10.11889/j.0253-3219
[16] R.C. Odom, R.W. Streeter, G.P. Hogan et al., A New 1. 625" Diameter Pulsed Neutron Capture And Inelastic/Capture Spectral Combination System Provides Answers In Complex Reservoirs. In: SPWLA 35th Annual Logging Symposium. (Oklahoma, 1994). doi:10.30632/SPWLA-1994-O
[17] M.P. Archer, R.C. Odom, R.D. Wilson et al., Pulsed Neutron Density Measurements: Modeling The Depth Of Investigation And Cased-Hole Wellbore Uncertainties. In: SPWLA 40th Annual Logging Symposium. (Norway, 1999). doi:10.30632/SPWLA-1999-JJ
[18] L. Jacobson, D. Durbin, S. Reed, An Improved Formation Density Measurement using PNC Tools. In: SPE Annual Technical Conference and Exhibition. (Texas, 2004). doi:10.2118/90708-MS
[19] Q.Y. Zhang, F. Zhang, J.T. Liu et al., A Method of Determining Formation Density Based on Fast-Neutron Gamma Coupled Field Theory. Petrophysics. **58** (04), 411-425 (2017). doi:10.30632/SPWLA-2017-v58n4a6
[20] M. Luycx, T.V. Carlos, Physics, applications, and limitations of borehole neutron-gamma density measurements. Geophysics. **84** (1), D39-D56 (2018). doi:10.1190/geo2018-0088.1
[21] H. Wang, W.S. Wu, R.G. Wang et al., Neutron transport correction and density calculation in the neutron-gamma density logging. Appl. Radiat. Isot. **150**, 110-119 (2019). doi:10.1016/j.apradiso.2019.05.023
[22] Q. Zhang, Source less density measurement using an adaptive neutron-induced gamma correction method. Nucl. Sci. Tech. **34**, 125 (2023). doi:10.1007/s41365-023-01274-4
[23] D.V. Ellis, J.M. Singer, Well Logging for Earth Scientists (Springer, 2007).
[24] X. Fu, W. Wu, H. Wang et al., A new neutron-gamma porosity measurement method for pulsed neutron logging tools. Geophysics. **88** (4), 1-55 (2023). doi:10.1190/geo2022-0471.1
[25] Q. Zhang, F. Zhang, C. Yuan et al., A comparative study on the neutron-gamma density and gamma-gamma density logging. J. Petrol. Sci. Eng. **176**, 792-799 (2019). doi:10.1016/j.petrol.2019.02.007
[26] S. Mahiout, A. Belowi, A. Alqunais et al., Impact of Improved Neutron-Gamma Density Measurement while Drilling in Formation Evaluation - A Case Study. In: SPE Annual Technical Conference and Exhibition. (UAE, 2016). doi:10.2118/181279-MS
[27] W. Tang, J.G. Liang, Y. Ge et al., A method for neutron-induced gamma spectra decomposition analysis based on Geant4 simulation. Nucl. Sci. Tech. **33**, 12 (2022). doi:10.1007/s41365-022-01144-5
[28] Q. Zhang, L.L. Lin, A fast forward computational method for nuclear measurement using volumetric detection constraints. Nucl. Sci. Tech. **35**, 31 (2024). doi:10.1007/s41365-024-01393-6
[29] W.C. Li, Q.X. Zhang, H.X. Wu et al., A gamma ray sourceless efficiency calibration method based on the Boolean operation of the ray deposition process. Appl. Radiat. Isot. **193**, 110620 (2023). doi:10.1016/j.apradiso.2022.110620
[30] W. Wu, N. Wei, L. Li, Quantitative analysis of neutron capture gamma-ray energy spectra using direct demodulation. Pet. Geosci. **79** (2), D91-D98 (2014). doi:10.1190/geo2013-0296.1
[31] Q.Y. Zhang, F. Zhang, C. Yuan et al., Application analysis on the different neutron gamma density (NGD) logging methods. Appl. Radiat. Isot. **172**, 109672 (2021). doi:10.1016/j.apradiso.2021.109672
[32] L. Zhang, H.W. Yu, W.B. Jia et al., Improved formation density measurement using controllable D-D neutron source and its lithological correction for porosity prediction. Nucl. Sci. Tech. **33**, 3 (2022). doi:10.1007/s41365-022-00988-1
[33] Y.L. Fu, Numerical Simulation of Pulse Neutron Density Logging Method and Tool Design, Northeast Petroleum University, 2019. doi:10.26995/d.cnki.gdqsc.2019.000451
[34] H. Wang, W.S. Wu, H.W. Wang et al., Formation density affects and corrections in pulsed neutron porosity logging. Nucl. Technol. **41** (08), 65-71 (2018). doi:10.11889/j.0253-3219.2018.hjs.41.080406
[35] S.F. Ajzenberg, Nuclear spectroscopy (Academic Press, 1960).
[36] K. Siegbahn, α, β, γ-ray spectroscopy (North-Holland Publishing Company, 1965).
[37] H.W. Yu, Z. Wang, Z.B. Xue et al., Corrections of fast neutron inelastic scattering effects on D-T neutron porosity logging. Appl. Radiat. Isot. **190**, 110486 (2022). doi:10.1016/J.APRADISO.2022.110486
[38] H. Wang, W.S. Wu, T.Z. Tang et al., A new method for calculating bulk density in pulsed neutron-gamma density logging. Geophysics. **85**, 06 (2018). doi:10.1190/geo2018-0821.1
[39] D. Dong, W.S. Wu, W.Z. Yue et al., Improving the pulsed neutron-gamma density method with machine learning regression algorithms. J. Petrol. Sci. Eng. **218**, 110962 (2022). doi:10.1016/j.petrol.2022.110962
[40] M.L. Mauborgne, R. Rodriguez, F. Allioli et al., Enhancing Accuracy and Range of Sourceless Density. In: SPWLA 65th Annual Logging Symposium. (Brazil, 2024). doi:10.30632/SPWLA-2024-0108